# Grain size reduction by plug flow in the wet oceanic upper mantle explains the asthenosphere's low seismic Q zone

Florence D.C. Ramirez [a,b,c,*], Clinton P. Conrad [a,c], Kate Selway [a,b,d]

[a] Centre for Earth Evolution and Dynamics, University of Oslo, Norway
[b] Department of Earth and Environmental Sciences, Macquarie University, Australia
[c] Centre for Planetary Habitability, University of Oslo, Norway
[d] Future Industries Institute, University of South Australia, Australia

## ABSTRACT

The prominent seismic low-velocity zone (LVZ) in the oceanic low-viscosity asthenosphere is approximately coincident with the low seismic Q zone (LQZ; a zone of high seismic attenuation). Small olivine grain sizes could link these seismic and rheological properties because they reduce viscosity, seismic velocity and seismic Q. Because rock deformation reduces grain sizes, the asthenosphere's seismic properties can place constraints on asthenospheric flow. To determine dominant flow patterns, we develop a self-consistent analytical 1-D channel flow model that accounts for upper mantle rheology and its dependence on flow-modified grain-sizes, water content, and melt fraction, for flow driven by both surface plate motions (Couette flow) and/or horizontal pressure gradients (Poiseuille flow). We find that Couette flow dominates if the upper mantle is dry, and plug flow (a Poiseuille flow for power law rheology) dominates if it is weakened by wet conditions. A plug flow configuration spanning the upper 670 km of the mantle best explains the LQZ in the asthenosphere, and can be attributed to significant grain-size reduction due to extensive shearing across the asthenosphere. This flow configuration also explains high seismic Q values below the asthenosphere associated with minimal shear deformation and large grain sizes above the mantle transition zone. We suggest that the asthenospheric LQZ and LVZ seismic anomalies can be largely explained by grain-size variations associated with plug flow in the wet upper mantle.

© 2023 The Author(s). Published by Elsevier B.V. This is an open access article under the CC BY license (http://creativecommons.org/licenses/by/4.0/).

## 1. Introduction

A seismic low-velocity zone (LVZ; Fig. 1) between $\sim 100 - 250$ km depth is a prominent feature below the oceanic lithosphere that is consistently reported by global and local seismological models (e.g., Dalton et al., 2009). Since the discovery of the LVZ by Gutenberg (1959), researchers have noted its overlap with the asthenosphere (Fig. 1), the low-viscosity zone that facilitates mantle deformation beneath the tectonic plates (e.g., Richards et al., 2001). Indeed, the deformation of asthenospheric rocks coincides with a seismically-anisotropic layer (high anisotropy zone, Fig. 1; e.g., Nettles and Dziewonski, 2008) that is produced by shear deformation of olivine (e.g., Tommasi et al., 1999; Jung and Karato, 2001). This deformation drives grain-size reduction (e.g., Behn et al., 2009), which can decrease both the seismic velocity (e.g., Faul

and Jackson, 2005) and the effective mantle viscosity (e.g., Warren and Hirth, 2006; Hirth and Kohlstedt, 2003), potentially amplifying the deformation. Stiff plates may also trap partial melt (e.g., Chantel et al., 2016; Selway and O'Donnell, 2019; Debayle et al., 2020), reducing seismic velocities (Hua et al., 2023).

In addition to reducing seismic wave speeds, both grain-size reduction and partial melt enhance the dissipation of seismic energy, and in fact the LVZ is approximately coincident with a zone of high seismic attenuation (low seismic quality factor Q), which we term here as the low Q zone or LQZ (Fig. 1). The LVZ, LQZ, and low viscosity asthenosphere all overlap (Fig. 1), and the coincident layer of seismic radial anisotropy suggests that all four are linked by asthenospheric deformation. Grain-size reduction, which is driven by rock deformation, is an obvious explanation, because it reduces seismic velocity, seismic Q, and effective viscosity. Indeed, without grain-size variations, the forward-prediction of seismic Q (Fig. S1, Supplementary Information) does not produce LQZ in the asthenosphere, and the relative amplitude of the LVZ is under-predicted. Patterns of rock deformation in the asthenosphere thus exert an important control on upper mantle seismic properties, and we can

---

\* Corresponding author at: Centre for Earth Evolution and Dynamics (CEED), University of Oslo, Sem Sælands vei 2A, 0371 Oslo, Norway.
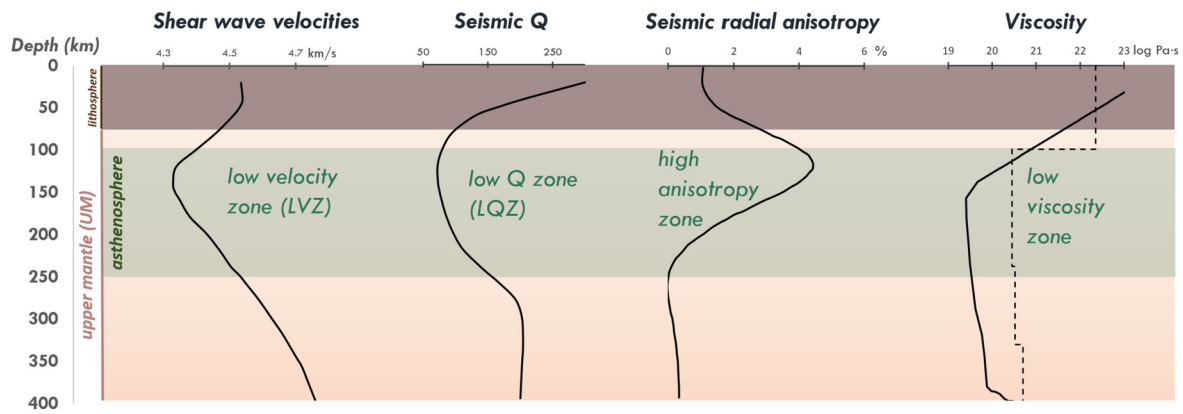*E-mail address:* f.d.c.ramirez@geo.uio.no (F.D.C. Ramirez).

**Fig. 1. Schematic representation of trends for seismic observations and inferred viscosities in the oceanic upper mantle** (above 400 km) where low shear wave velocity, low seismic Q, high radial anisotropy, and low viscosity exist within the same approximate depth range (the asthenosphere, green region). The shear wave velocity model shown is from Nettles and Dziewonski (2008) for 25-100 Myr oceanic plate ages, the global seismic Q factor (in linear scale) is from Karaoglu and Romanowicz (2018), and the global seismic radial anisotropy (in %) is from Nettles and Dziewonski (2008) for mid-age oceans. The viscosity profiles (in logarithmic scale) are inferred from mantle flow models where the solid line is for purely temperature-dependent viscosity (Becker, 2006), and the dashed line is geoid-constrained viscosity (Steinberger and Calderwood, 2006).

use seismic observations of the LVZ and LQZ to constrain asthenospheric deformation models.

Using grain size evolution models (e.g., Austin and Evans, 2007; Hall and Parmentier, 2003), we investigate depth variations in grain size resulting from flow-induced deformation within the upper mantle. Behn et al. (2009) already demonstrated the importance of grain size evolution for seismic depth profiles associated with Couette flow (Fig. 2a), which describes asthenospheric shear driven by surface plate motion. However, recent studies have suggested that Poiseuille flow (Fig. 2b), driven by lateral pressure gradients associated with mantle upwellings and downwellings, may be the dominant deformation mode within much of the upper mantle (e.g., Höink and Lenardic, 2010; Semple and Lenardic, 2018). Here we develop an analytical model that can incorporate both Couette and Poiseuille flows, and use it to determine how grain-size variations depend on flow drivers such as plate speed and horizontal pressure gradient, and on mantle parameters such as melt fraction and particularly water content (Fig. 2c). In particular, we investigate feedbacks between grain-size, rheology, and asthenospheric flow configuration. From the modeled flow in the upper mantle, we make predictions of seismic depth profiles that can be tested against observations of seismic velocity and attenuation (Fig. 2c). This comparison places constraints on mantle conditions and the dominant flow types necessary to explain the observed LVZ and LQZ.

## 2. Types of flow in the oceanic upper mantle

Several analytical and numerical studies show that flow in the upper mantle results from a combination of Couette (plate-driven, Fig. 2a) and Poiseuille (pressure- driven, Fig. 2b) flows (e.g., Höink and Lenardic, 2010; Natarov and Conrad, 2012). Couette flow (abbreviated as *CF* here) can operate with Newtonian and/or power law rheology via diffusion and/or dislocation creep, respectively (e.g., Podolefsky et al., 2004). If Couette flow occurs via dislocation creep, this shearing flow produces a lattice-preferred orientation (LPO) of olivine crystals that form a single seismically anisotropic layer (Fig. 2a). Two distinct anisotropic layers, as detected by Lin et al. (2016) at the top and the base of the Central Pacific asthenosphere, can be formed by separate shear zones if the asthenosphere additionally hosts Poiseuille flow (abbreviated *PF*, Fig. 2b). This flow is driven by a significant horizontal pressure gradient and results in Newtonian Poiseuille flow (*PFn1*, Fig. 2b.1) for diffusion creep and so-called "plug flow" (*PFn3*, Fig. 2b.2) for dislocation creep (here we abbreviate the style of Poiseuille flow with the rhe-

ological power-law stress exponent $n$: e.g., *PFn3* indicates Poiseuille flow with $n = 3$). Plug flow has approximately uniform velocity in the middle of the low-viscosity layer, bounded above and below by zones of intense shear deformation (Semple and Lenardic, 2018).

## 3. Analytical plate- and pressure-driven flow model for the oceanic upper mantle

To investigate the effect of flow configurations on rheology (Section 4) and seismic depth profiles (Section 5), we develop an analytical 1-D channel flow model for the oceanic mantle. We let the rheology of the mantle determine the style of flow and the associated flow rates and stresses (Section 3.2). The flow alters the olivine grain size with time until the size stabilizes (Section 3.3). This temporal evolution of olivine grain size requires us to also calculate the time-evolution of the shear stresses, horizontal velocities and viscosities (Section 3.4). From this, we can account for possible feedbacks between flow configuration, rheology, deformation, and grain-size.

### 3.1. Model Set-up

Since we do not know the appropriate depth and the velocity boundary condition at the base of the asthenosphere (green region, Fig. 1), we incorporate the entire oceanic mantle down to 670 km into our model (Fig. 2d). We impose a plate speed $U_p$ at 0 km to drive *CF* (Fig. 2a), and a zero flow condition ($v_x = 0$) at 670 km, which assumes that flow is much slower in the highly viscous lower mantle. We assign the same lateral pressure gradient ($dp/dx$) across all layers above 670 km, which drives *PF* (Fig. 2b). From the $U_p$ and $dp/dx$ drivers, the resulting flow configuration and the associated flow velocities ($v_x$) are determined by the composite rheology above 410 km, and the assigned Newtonian rheology of the mantle transition zone (Fig. 2c and Section 3.2). The rheology above 410 km is dictated by the assigned water content (50 ppm H/Si or 1000 ppm H/Si) and melt fraction, the computed geotherm for a 60 Myr oceanic plate with 1623 K potential temperature (Fig. 2d; using Equation 4.113 of Turcotte and Schubert (2014)), and the deformation-dependent olivine grain size. This results in a cold and highly viscous lithosphere at depths shallower than ~100 km and a deformable upper mantle layer between the lithosphere and the mantle transition zone (MTZ; 410 – 670 km). Although the MTZ may deform under dislocation creep (e.g., Ritterbex et al., 2020), we assigned a Newtonian viscosity in the range $10^{19} - 10^{21}$ Pa·s, reflecting geophysical estimates (e.g., Kaufmann
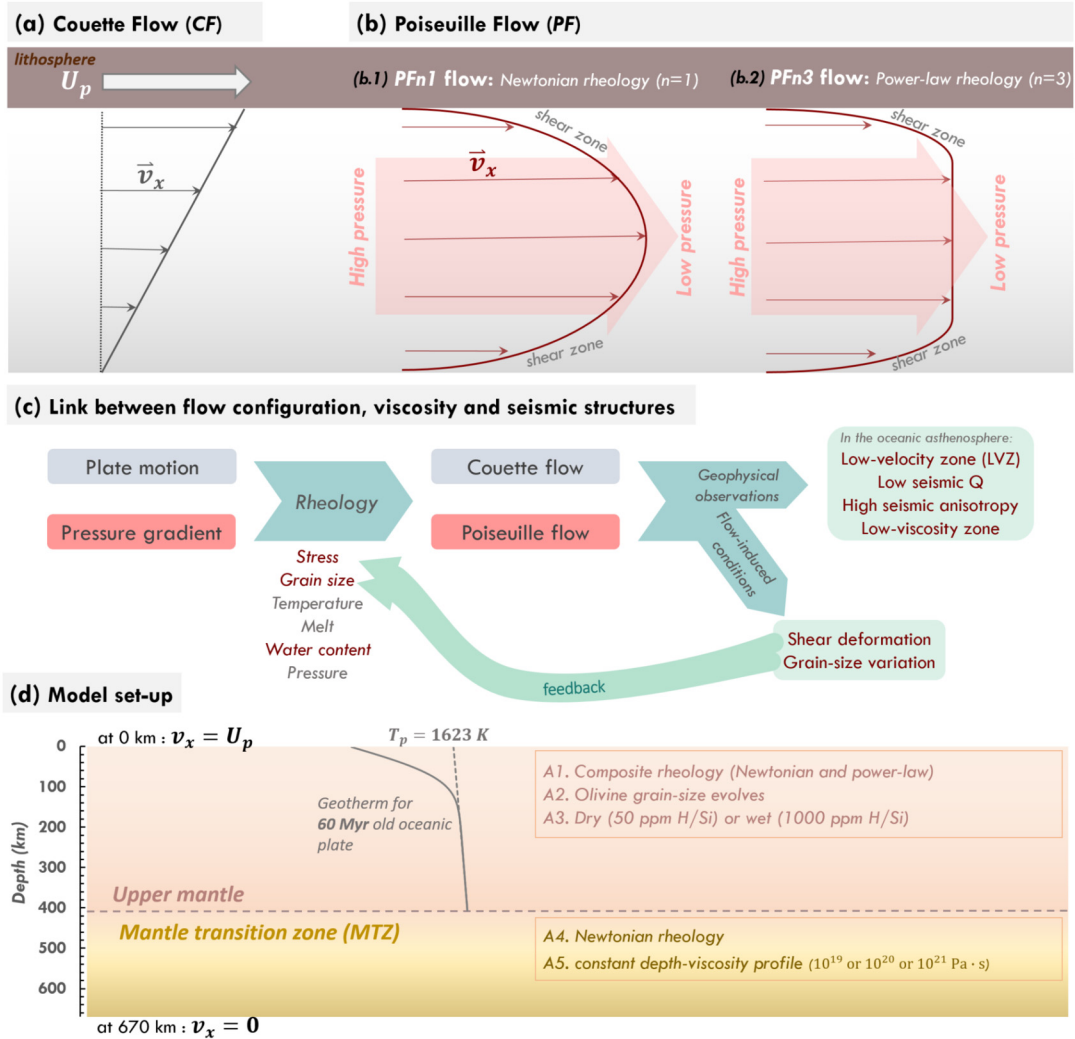
**Fig. 2. (a-b) Dominant flow regimes in the upper mantle:** Sketch of flow velocities ($\vec{v}_x$) due to (a) Couette flow (*CF*) driven by surface plate motion and (b) Poiseuille flow (*PF*) driven by a lateral pressure gradient. The rheology of the upper mantle determines the *PF* configuration, where (b.1) a parabolic-shaped velocity profile arises if the rheology is Newtonian (termed *PFn1* here), or (b.2) a plug flow arises for power-law rheology (termed *PFn3* here). **(c) Simple flow chart that links geodynamic drivers (left), flow regimes (middle) and seismic structures (right) in the asthenosphere.** The dominant flow regime is dictated by rheology, which is controlled by the enumerated parameters. Feedback arrow indicates parameters that are affected by the flow deformation itself. Most of the rheological parameters also affect seismic structures, which provide geophysical constraints. Red texts indicate target parameters in this study. **(d) Model set-up.** We consider a 60 Myr old oceanic plate with 1623 K potential temperature ($T_p$) that results in a temperature profile shown in (d). We assume that the oceanic upper mantle (defined here as the region above 410 km) is governed by a composite olivine rheology, which is controlled by the geotherm, grain sizes and water content (dry or wet). We also consider the mantle transition zone (MTZ, 410 – 670 km) in our analytical model to investigate its effect on the flow configurations within the upper mantle region above it. Since its rheology is not well constrained by experiments, we assume a Newtonian and constant viscosity for the MTZ. Given the calculated (above 410 km) and assigned (for the MTZ) rheologies, flow velocities are computed using Equations (7.2) and S9, where the boundary conditions are shown in (d).

and Lambeck, 2000; Forte and Mitrovica, 1996). We did not calculate MTZ viscosity for different mantle parameters such as water content and grain size because the flow laws for ringwoodite and wadsleyite (polymorphs of olivine that are stable in the MTZ) are not well constrained by experiments.

### 3.2. Working equations for the 1D flow model

In this study, we solve for *PF* configurations, but with a velocity boundary condition associated with *CF* (Fig. 2d). We use the Navier-Stokes equation for combined plate- and pressure-driven flows:

$$\rho \frac{D\vec{v}}{Dt} = -\nabla p + \vec{F} + \eta \nabla^2 \vec{v} \tag{1}$$

Neglecting the inertial term $\frac{D\vec{v}}{Dt}$ and body forces $\vec{F}$ gives pressure and viscous terms for a 1D model,

$$-\frac{\partial p}{\partial x} + \frac{\partial}{\partial z}\left(\eta(z)\frac{\partial v_x}{\partial z}\right) = 0 \tag{2.1}$$

$$-\frac{\partial p}{\partial x} + \frac{\partial}{\partial z}(\tau_{xz}) = 0 \tag{2.2}$$

where $\frac{\partial p}{\partial x}$ is a constant horizontal pressure gradient, $\eta(z)$ is depth-dependent viscosity, $\tau_{xz}$ is the shear stress, and $v_x$ is the horizontal velocity (either plate-driven or pressure-driven). Integrating Equation (2.2) with respect to $z$ yields an estimate of the shear stress $\tau_{xz} = \tau$ induced by the flow at every layer $i$ of our 1D model as described by

$$\tau_i = \frac{\partial p}{\partial x} z_i + C_i \tag{3}$$

where $C_i$ is a constant of integration. When $\frac{\partial p}{\partial x} = 0$, Equation (3) simplifies into a constant stress, which describes a *CF* configuration.

When assuming a composite rheology (that is, rheology controlled by both diffusion and dislocation creep), the total strain rate (Hirth and Kohlstedt, 1996) per layer is

$$\dot{\varepsilon}_{total,i} = \dot{\varepsilon}_{diff,i} + \dot{\varepsilon}_{disl,i} = \frac{\sigma}{\eta_{eff,i}} \tag{4}$$

where $\dot{\varepsilon}_{diff}$ is the strain rate for diffusion creep, $\dot{\varepsilon}_{disl}$ is the strain rate for dislocation creep, $\eta_{eff}$ is the effective viscosity, and $\sigma$ is the differential stress which is equivalent to $2\tau$. The strain-rate components are defined according to their relevant rheological relationships,

$$\dot{\varepsilon}_{diff,i} = A_{PFn1,i}\tau_i = \frac{\partial v_{PFn1,i}}{\partial z} \tag{5.1}$$

$$\dot{\varepsilon}_{disl,i} = A_{PFn3,i}\tau_i^3 = \frac{\partial v_{PFn3,i}}{\partial z} \tag{5.2}$$

$$A_{PFn1,i} = A_{diff}C_{OH}^{r_{diff}}d^{-p_{diff}}\exp(\propto_{diff}\varphi)\exp\left[-\frac{E_{diff}+PV_{diff}}{RT}\right] \tag{5.3}$$

$$A_{PFn3,i} = A_{disl}C_{OH}^{r_{disl}}d^{-p_{disl}}\exp(\propto_{disl}\varphi)\exp\left[-\frac{E_{disl}+PV_{disl}}{RT}\right] \tag{5.4}$$

which express the empirically determined flow laws (Hirth and Kohlstedt, 2003). The velocities $v_{PFn1,i}$ and $v_{PFn3,i}$ in Equations (5.1) and (5.2) are the horizontal velocities for *PFn1* and *PFn3* flow configurations, respectively. The upper mantle parameters defined in Equations (5.3) and (5.4) prescribe the rheological impact of grain-size $d$, water content $C_{OH}$, and melt fraction $\varphi$ (other parameters are defined in Table S1; Supplementary Information). Dislocation creep and thus $v_{PFn3}$ are strongly stress-dependent with stress exponent of 3 (Equation (5.2)). Diffusion creep and $v_{PFn1}$ are significantly controlled by grain size with an exponent $p_{diff} = 3$ (Equation (5.3)), while $p_{disl} = 0$ for dislocation creep (Equation (5.4)). Therefore, we expect that weak stresses (i.e., <1 MPa) and small grain sizes (i.e., <3 mm) favor diffusion creep and *PFn1* flow, whereas strong stresses and big grain sizes result in dislocation creep and *PFn3* flow. Water content is important, as wet upper mantle with large grain sizes may favor dislocation creep (Ramirez et al., 2022) and *PFn3* flow, even for weak stresses. Together, these factors combine to yield an effective viscosity $\eta_{eff}$

$$\eta_{eff} = \frac{2}{A_{PFn1,i} + A_{PFn3,i}\tau_i^2} \tag{6}$$

that depends on stress, grain size and water content according to Equations (5.3) and (5.4). For the deeper MTZ layer we assign a Newtonian rheology $\eta_{MTZ}$, which we implement using $A_{PFn1,i} = 2/\eta_{MTZ}$ and $A_{PFn3,i} = 0$.

The overall $v_{x,i}$ is $v_{PFn1,i} + v_{PFn3,i}$, where the velocity components are integrals of Equations (5.1) and (5.2) with respect to $z$, respectively:

$$v_{x,i} = \int A_{PFn1,i}\tau_i dz + \int A_{PFn3,i}\tau_i^3 dz \tag{7.1}$$

Substituting $\tau_i$ from Equation (3) into Equation (7.1), and integrating with respect to $z$ yields:

$$v_{x,i} = A_{PFn1,i}\left[\frac{1}{2}\frac{\partial p}{\partial x}z_i^2 + C_i z_i\right]$$
$$+ A_{PFn3,i}\left[\begin{array}{l}\frac{1}{4}\left(\frac{\partial p}{\partial x}\right)^3 z_i^4 + C_i\left(\frac{\partial p}{\partial x}\right)^2 z_i^3 \\ + \frac{3}{2}C_i^2\frac{\partial p}{\partial x}z_i^2 + C_i^3 z_i\end{array}\right] + k_i \tag{7.2}$$

where $k_i$ is the constant of integration and the involved parameters are summarized in Supplementary Table S1. For $\frac{\partial p}{\partial x} = 0$, Equation (7.2) describes a *CF* configuration.

Implementing the necessary boundary conditions and linearizing the problem as described in Supplementary Information C, we estimate the horizontal velocities (Equation (7.2)) and shear stresses (Equation (3)) that are determined by mantle parameters (i.e., grain sizes, water content) and flow drivers (i.e., plate velocity, pressure gradient), while including feedbacks from stress and grain size (Fig. 2c).

### 3.3. Olivine grain size evolution model for the upper mantle

During deformation, mineral grain sizes evolve according to:

$$\dot{d} = \dot{d}_{gg} - \dot{d}_{dr} \tag{8}$$

If the grain growth rate $\dot{d}_{gg}$ equilibrates with the rate of grain reduction by dynamic recrystallization $\dot{d}_{dr}$, then $\dot{d} = 0$ and grain size is stable. We mainly employ the grain-size evolution model of Austin and Evans (2007) (AE07), where the expressions for $\dot{d}_{gg}$ and $\dot{d}_{dr}$ are described in Equation S16 with parameter values from Supplementary Table S1. As deformation proceeds, new grain boundaries are created ($\dot{d}_{dr} > 0$), resulting in grain size reduction. Because larger grains are subdivided faster than smaller grains, grain size reduction rates increase with grain size (second term, Equation S16). Dislocation creep is the dominant mechanism that creates new grain boundaries and thus controls grain-size reduction rates. At depths with minimum stress, water promotes grain growth through significant reduction in dislocation strain rate, which causes grains to grow until otherwise restricted (e.g., pinning by other minerals). We also tested the grain-size evolution model of Hall and Parmentier (2003) (HP03) as shown in Supplementary Fig. S5, which illustrates that both HP03 and AE07 models provide similar steady-state flow configurations and rheology.

### 3.4. Temporal evolution of olivine grain-size, rheology and flow configuration

Using the set-up described above and in Supplementary Information C, D and E, we investigate how the flow configuration, shear stress, rheology, and deformation evolve with time in the oceanic mantle (Fig. 3). Here we consider a 10 cm/yr plate velocity and −5 kPa/km pressure gradient across dry (50 ppm H/Si) upper mantle and a $10^{21}$ Pa·s MTZ. Initially (0 yr), we assume a constant small grain-size of 1 mm, which induces low effective viscosity (Fig. 3e) under diffusion creep (Equation (5.2)). A large pressure gradient (−5 kPa/km) deforms this low-viscosity mantle with a *PFn1* configuration (Fig. 3b). However, within tens of years olivine grain-sizes grow (Fig. 3a) as the flow-driven deformation evolves to a steady-state structure (Fig. 3d). This occurs because grain growth rates are faster than grain-size reduction rates during the initial diffusion creep regime (Section 3.3). This grain growth initiates dislocation creep (Fig. 3f) and increases effective viscosity (Fig. 3e), which slows pressure-driven flow in favor of plate-driven *CF* (Fig. 3b). We find that steady state is reached after only 152 kyr (only 0.3% of the plate age), which is significantly faster than mantle flow time scales. This indicates that grain size is always in effective equilibrium for steady-state mantle flow problems, and that adjustments associated with grain-size evolution (Fig. 3) can be considered essentially instantaneous.

Although the initial grain size does not affect the final, steady-state grain size (Supplementary Information F.1), the choice of initial grain size does affect the time for the grain size to stabilize (Supplementary Fig. S4). A larger initial grain size (e.g., 10 mm) stabilizes faster than a smaller grain size (1 mm), because large
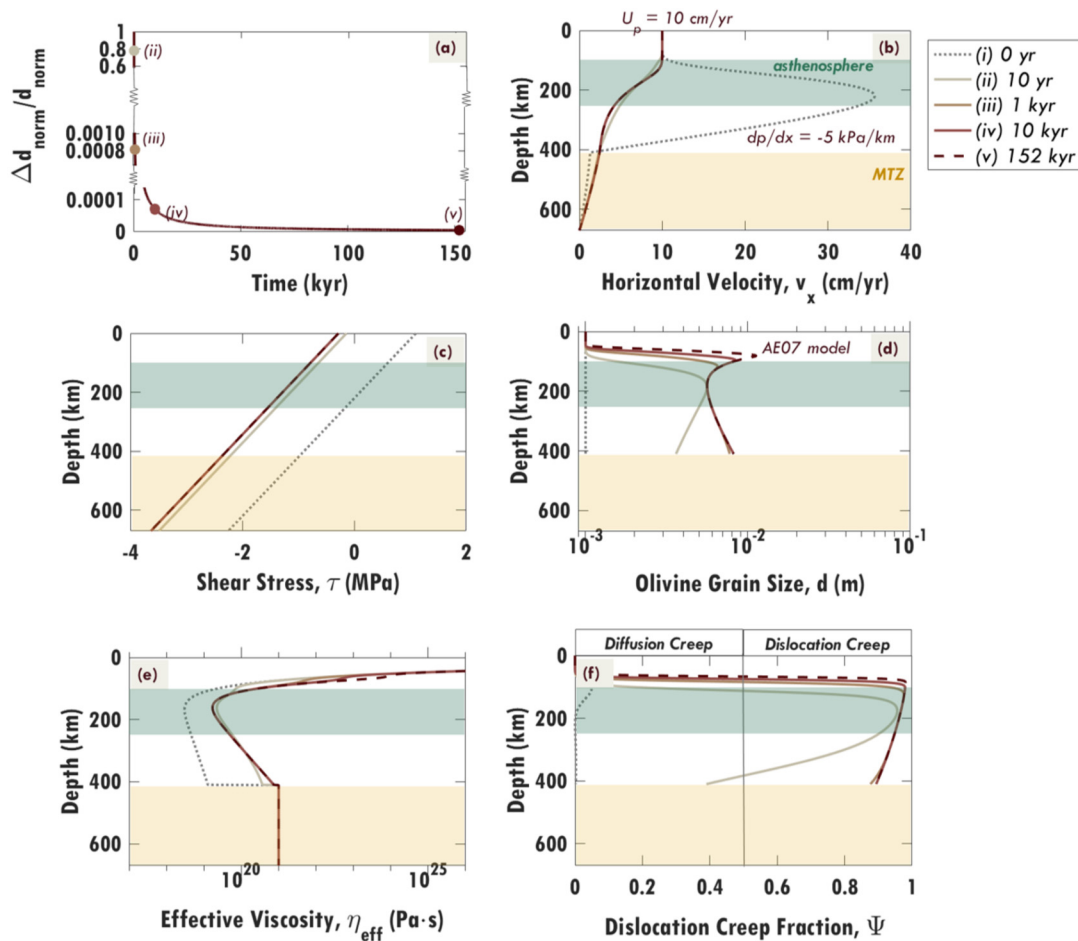
**Fig. 3. Temporal evolution of flow with an imposed pressure gradient (−5 kPa/km) and plate velocity (10 cm/yr).** The upper mantle (above 410 km) is dry (50 ppm H/Si) and has an initial (at 0 yr) constant (1 mm) olivine grain-size. The mantle transition zone (MTZ, yellow region, 410-670 km) with a viscosity of $10^{21}$ Pa·s is assumed to deform together with the upper mantle. During the deformation induced by the flow (b), olivine grain-sizes evolve (d) following the AE07 model (Austin and Evans, 2007) as in Equation (8) or S16 with an activation volume for grain growth of $V_g = 4 \times 10^{-6}$ m³/mol. The grain-size structure stabilizes after 152 kyr, as shown in (a) by the time evolution of the convergence criterion ($\Delta d_{norm}/d_{norm}$ for timestep $\Delta t$ = 10 yr; Supplementary Information E). The flow configuration (b), shear stress profiles (c), effective viscosity (e) and the deformation type (f) all evolve and stabilize as a result. The initially *PFn1* flow (dotted line; Newtonian Poiseuille flow) becomes dominantly *CF* (Couette flow) because the increased grain-size (d) increases upper mantle viscosity (e). Note that a low viscosity zone (e) forms at asthenospheric depths (100–250 km, highlighted in green).

grains subdivide more rapidly than small grains, which tend to grow before subdividing (Equation S16). In the following section, we assume an initial grain size of 10 mm because it reaches steady state faster and thus reduces calculation time.

## 4. Effect of flow drivers and rheology on oceanic upper mantle flow configurations

Here, we investigate how grain-size, water content, the imposed plate velocity and the horizontal pressure gradient control the dominant flow configuration of the upper mantle (Fig. 2c and Fig. 4). We consider both dry (50 ppm H/Si) and wet (1000 ppm H/Si) conditions for layers above the MTZ, and assign $10^{21}$ Pa·s for MTZ viscosity if the upper mantle is dry and $10^{20}$ Pa·s if it is wet. This setup maintains comparable effective viscosities for the upper mantle and MTZ layers, and we investigate flow configurations for contrasting rheologies later (Section 7). To consider a range of flow drivers, we vary the plate velocity between 0 and 10 cm/yr in the direction of pressure-driven flow, and horizontal pressure gradients between 0 and −5 kPa/km (e.g., Natarov and Conrad, 2012).

Steady-state grain sizes determine the dominant deformation mechanism and viscosity in the oceanic upper mantle, and thus the pattern of flow there (Section 3.4, Fig. 3). For sufficiently large

pressure gradients, *PFn1* and *PFn3* flow types occur in diffusion creep (small grain size) and dislocation creep (large grain size) regimes, respectively. In contrast, *CF* dominates if the pressure gradient is too weak to cause deformation, regardless of the dominant deformation mechanism. In both cases, the viscosity of the upper mantle determines whether *PF* or *CF* dominates for a given pressure gradient and plate velocity setup. This implies that increasing the strength of a flow driver might not induce a change in flow type (e.g., increasing the pressure gradient in a *CF*-dominated mantle; case i vs. ii, Fig. 4a), unless the viscosity structure permits it (e.g., case i vs. ii, Fig. S6d).

The water content of the upper mantle controls rheology both directly via weaker minerals and indirectly via grain-size evolution, and thus determines the type of flow. We find that if water is present in the upper mantle, *PFn3* is likely to dominate (Fig. 4d). Otherwise, *CF* dominates (Fig. 4a) because the higher viscosities associated with a dry upper mantle do not permit Poiseuille flow. As a feedback mechanism, the flow configuration dictates the grain-size structure and thus also the viscosity structure. If the upper mantle is *PFn3*-dominated (Fig. 4d), a viscosity peak (Fig. 4f) develops, associated with both slow deformation (Semple and Lenardic, 2018) and large grain-sizes (Fig. 4e). Deformation in the mid-upper mantle is slow because plug flow (*PFn3*) features approximately
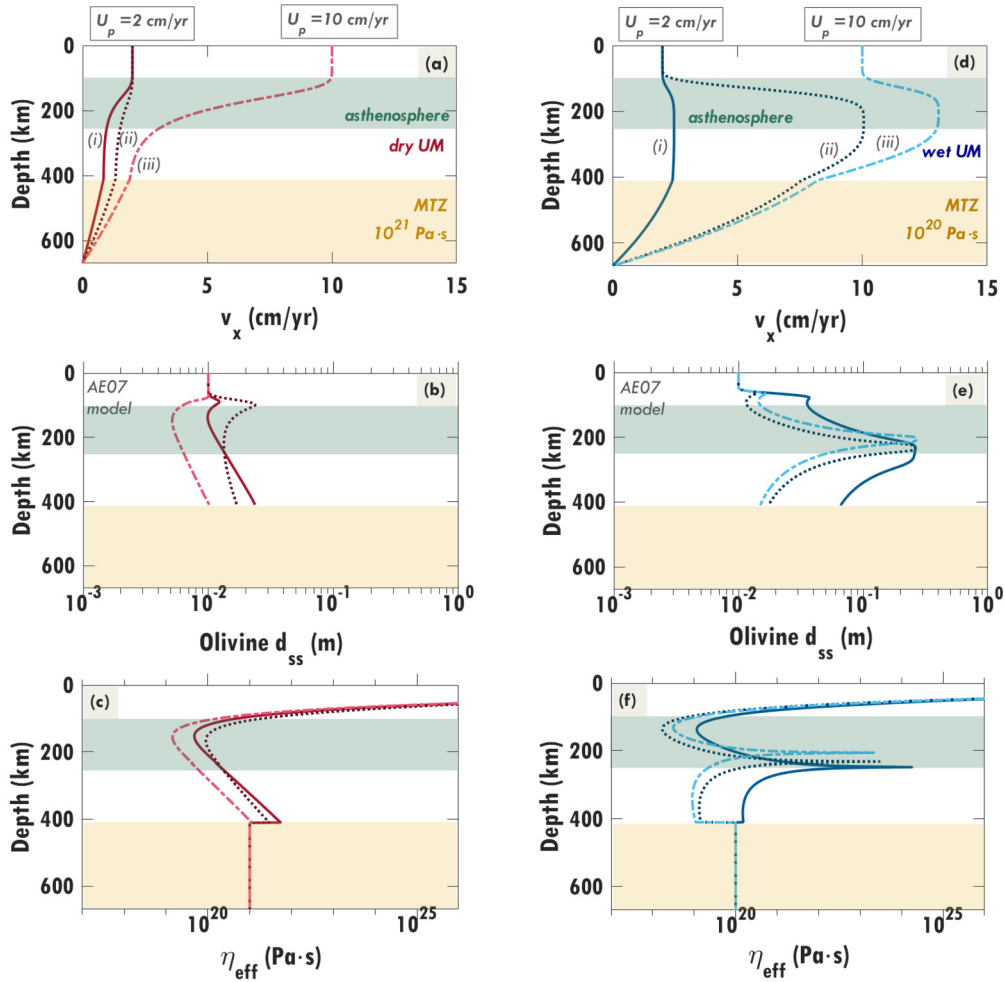
**Fig. 4. Factors affecting upper mantle flow (a, d), grain-size (b, e), and viscosity (c, f) at steady state for dry (a-c) and wet (d-f) conditions.** Different combinations of imposed plate velocity and horizontal pressure gradient (labeled as i, ii and iii) are considered, where $U_p$ and $\partial p/\partial x$ are (i) 2 cm/yr and $-1$ kPa/km, (ii) 2 cm/yr and $-3$ kPa/km, and (iii) 10 cm/yr and $-3$ kPa/km. Dry upper mantle (50 ppm H/Si) flows via *CF* (a) while wet upper mantle (1000 ppm H/Si) flows via *PFn3* (d). Nonetheless, grain size reduction in the asthenosphere (b, e) results in a low viscosity zone (c, f). *PFn3* deformation is minimal near the bottom asthenosphere (d), leading to grain growth (e) because of small flow-induced stresses. Both small stresses and large grains contribute to a peak in effective viscosity (f; Equation (6)).

constant horizontal velocities, resulting in minimal shear stresses (Fig. S5b) that enhance effective viscosity associated with dislocation creep (Equations (5.4) and (6)). The slow deformation also hinders grain-size reduction (second term, Equations (8) and S16), leading to large grains that enhance the viscosity associated with diffusion creep (Equations (5.3) and (6)). Extensive shearing above and below the non-deforming region results in significant grain-size and viscosity reduction in both the shallow and deep upper mantle. In contrast, a *CF*-dominated upper mantle (Fig. 4a), which is more typical of dry conditions, features grain-sizes (Fig. 4b) and viscosity (Fig. 4c) that gradually increase with depth. Regardless of the flow configuration, grain-size reduction and the associated rapid deformation control the low viscosity zone in the asthenosphere.

In general, an increase in either the plate velocity (case ii vs. iii, Fig. 4a) or the pressure gradient magnitude (case i vs. ii, Fig. 4d) increases the stress induced by the flow. The resulting increase in stress reduces viscosity (Equation (6)) and grain-sizes (Equation S16) further, which in some cases may amplify deformation and make diffusion creep important ($\Psi < 1$). However, in our forward models, grain sizes remain larger than $\sim 3$ mm (as in Fig. 3d), which is large enough for dislocation creep to remain dominant (e.g., Fig. 3f).

## 5. Predicted seismic depth profiles for dry and wet oceanic upper mantle

To quantify the impact of flow configurations on the upper mantle seismic depth profile, we estimate the shear wave velocity $V_s$, the seismic Q factor, and seismic anisotropy based on rates of dislocation strain for the steady-state grain sizes associated with the different plate velocity and pressure-gradient combinations considered in Section 4. We estimate $V_s$ following the Q-dependent formulation of Karato (1993; Equation S1). We calculate the seismic Q using the grain-size dependent formulation of Jackson and Faul (2010) and approximate period (s) = depth (km)/1.4, which is appropriate for surface waves (Forsyth, 1992). The experimentally-constrained impact of water content on seismic attenuation is still debated, and may be significant (e.g., Karato and Jung, 1998; Karato, 2012) or not (e.g., Cline et al., 2018). Here we consider the direct effect of water on viscosity and grain size evolution, the latter of which affects seismic Q and $V_s$.

### 5.1. Effect of water content and flow configuration on seismic depth profiles

Different grain size structures for dry (Fig. 4b) and wet (Fig. 4e) conditions result in different depth profiles for seismic Q (Figs. 5a
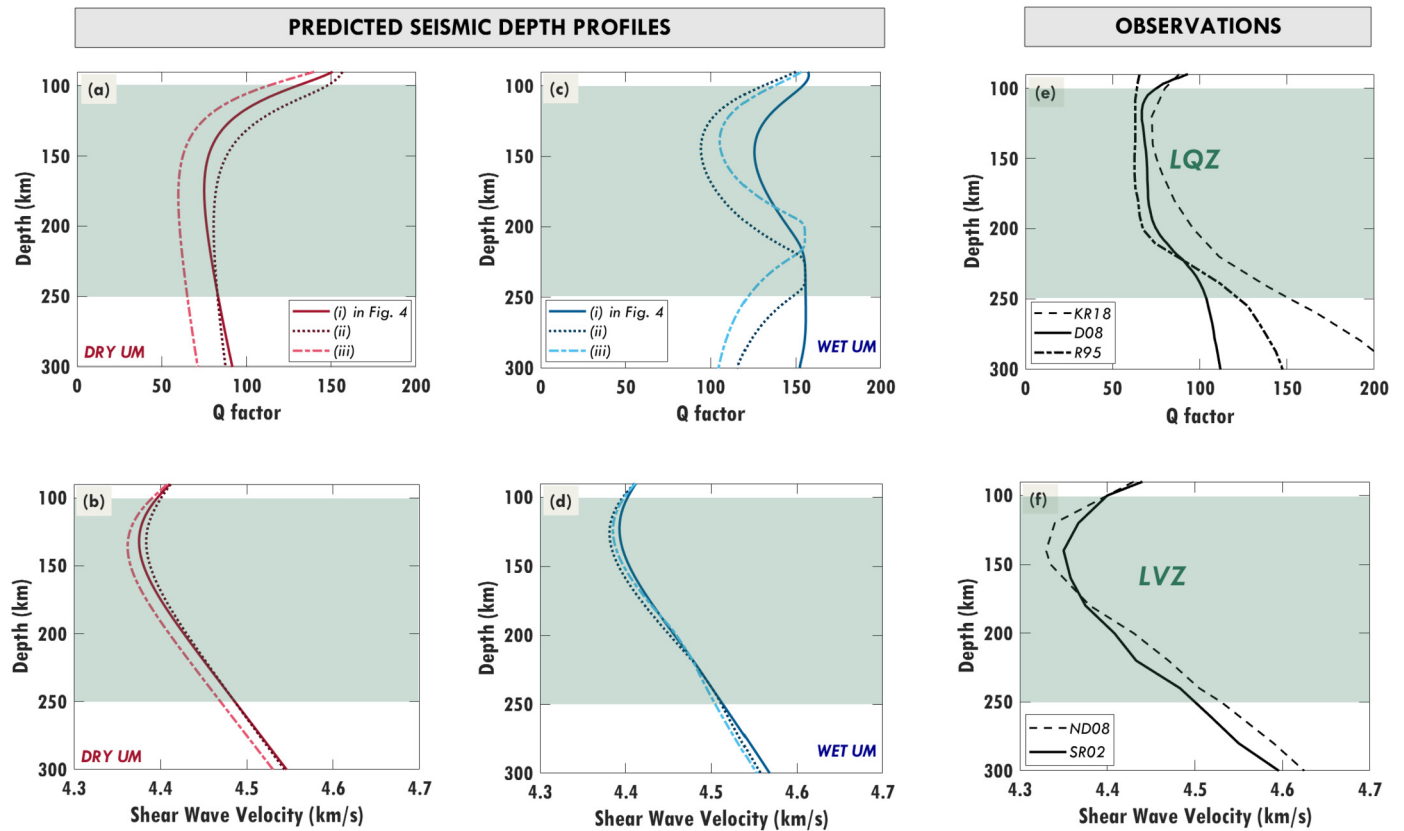
**Fig. 5. (a-d) Predicted seismic depth profiles**, computed for cases (i) to (iii) from Fig. 4. The forward Q values for dry (a) and wet (c) conditions are calculated using the steady-state grain sizes in Figs. 4b and 4e, as are the forward shear wave velocity depth profiles (b and d). **(e) Observations of the low seismic Q zone (LQZ)** for comparison are the KR18 and R95 global Q models of Karaoglu and Romanowicz (2018) and Romanowicz (1995), respectively, and the D08 model of Dalton et al. (2008) for mid-age oceans. **(f) Observations of the low seismic velocity zone (LVZ)** for comparison are the ND08 velocity model of Nettles and Dziewonski (2008) for 25–100 Myr old oceanic plate ages and SR02 model of Shapiro and Ritzwoller (2002) for 75 Myr seafloor age. The green region indicates the seismically anomalous asthenosphere (100–250 km depth) identified in Fig. 1. All forward models show local minima of the respective seismic property in the asthenosphere, but the LQZ is more evident within wet upper mantle (c).

and 5c) and shear wave speeds (Figs. 5b and 5d). Thus, water content indirectly, but significantly, impacts seismic signatures via flow-affected grain-size evolution. Notably, although we can produce the seismic shear wave trends of the LVZ regardless of the water content and flow configuration, this is not true for the LQZ in the asthenosphere. For dry upper mantle flowing via *CF*, the forward model (Fig. 5a) shows a sharp drop in Q at the top asthenosphere followed by a gradual increase in Q with depth because of increasing grain size (Fig. 4b). In contrast, a wet upper mantle deformed via *PFn3* produces a well-pronounced LQZ in the asthenosphere (Fig. 5c). Apart from the effect of activation volume (Supplementary Information B and Fig. S2d), the magnitude and extent of this zone are determined by the plate velocity and pressure gradient combination because the grain size evolution is stress-dependent. Indeed, the grain-size structure produced by the *PFn3* configuration affects the Q-depth profile and only minimally changes the $V_s$-depth profile. For instance, the Q peak within the lower asthenosphere (200–250 km) is caused by the grain-size peak (Fig. 4e) associated with weak shearing in this region. However, this is not evident for *CF*-dominated dry asthenosphere because the grain size increase is much smaller (Fig. 4b).

*5.2. Comparing predicted seismic Q and $V_S$ with observations*

Reported Q models (Fig. 5e) are often globally-averaged profiles, which limits spatial resolution and may cancel out some localized features, complicating comparisons to regional observations (Section 6.3). The shear wave velocity observations presented

here are averaged for oceanic plates of similar ages (i.e., mid-age plates, Fig. 5f), and thus should be comparable with our curves for an assumed 60 Myr old oceanic plate (Figs. 5b and 5d). However, because of averaging across plates with different speeds and pressure gradients, we are limited in our comparisons between predicted and observed Q and $V_S$, which assume single choices of these parameters. Instead, we compare overall trends between the theoretical and geophysical models, and later attempt to infer the dominant type of flow in the oceanic upper mantle from the seismic observations (Section 7).

Although the *PFn3* configuration produces the LQZ, the predicted minimum Q (Fig. 5c) is consistently larger (by $\Delta Q \sim 20 -$ 50) than observed (Fig. 5e) because of large predicted grain sizes ($>10$ mm) in wet conditions. Dry conditions can result in smaller grain sizes and reduced Q (Fig. 5a), but the LQZ only forms if the mantle is *PFn3*-dominated (see Section 7). Reduced Q in the asthenosphere may also result from a larger activation volume for grain growth $V_g$ (Fig. S2d), or small amounts of melt (Fig. 6). The observed large Q ($>100$) below the asthenosphere requires a *PFn3* configuration that spans the upper 670 km depth (i.e., case i, Fig. 4d), and not confined to the upper mantle above 410 km (as for cases ii and iii). This specific flow configuration results in large grain sizes below the asthenosphere associated with weak shearing in this region (Fig. 4e and Section 7).

We investigate the impact of partial melt on the predicted seismic depth profiles by assuming a melt distribution scenario in the asthenosphere (Fig. 6a, $x - 0.10\%$) where $x$ in % is estimated from Debayle et al. (2020) models for a plate moving with a speed
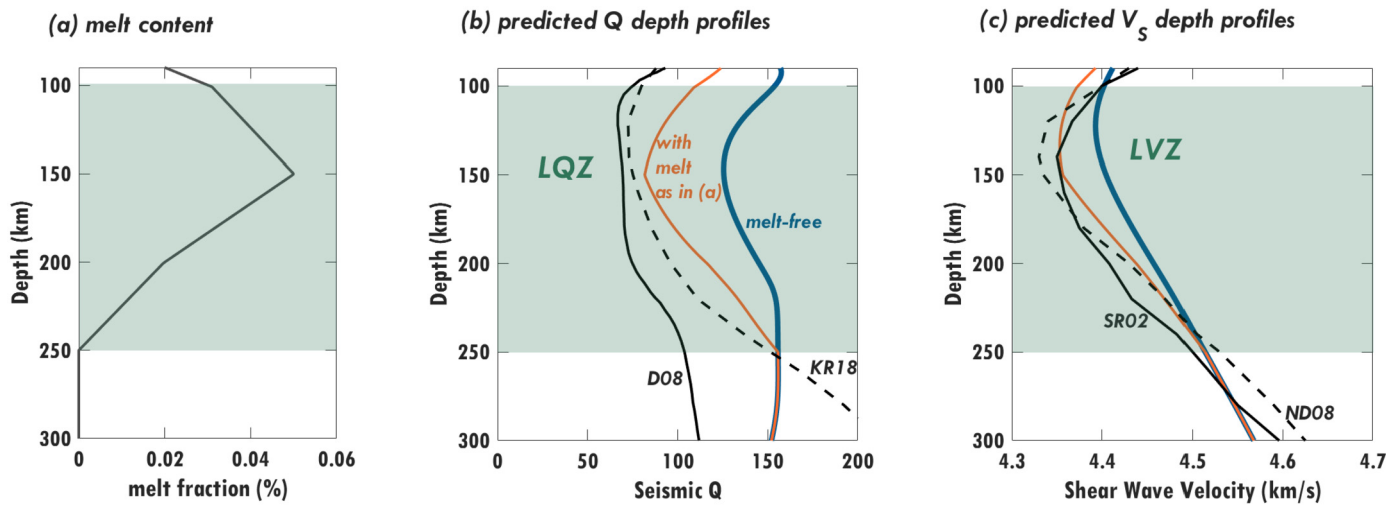
**Fig. 6. Impact of (a) partial melt distribution on predicted zones of low seismic (b) Q (LQZ) and (c) $V_S$ (LVZ).** The melt fraction in the asthenosphere (a) is calculated as $x - 0.10\%$ where $x$ (in %) is estimated from Debayle et al. (2020) models for a plate moving with a speed of 2 cm/yr. The Jackson and Faul (2010) formulation for Q is used to predict seismic Q depth profiles (blue lines in (b) and (c)) for a melt-free and wet (1000 ppm H/Si) upper mantle deforming beneath an oceanic plate moving with a speed of 2 cm/yr above a $-1$ kPa/km pressure gradient (case i, Fig. 4d) and associated flow-induced grain sizes (Fig. S7b). If melt from (a) is present, both seismic Q and $V_S$ are reduced (orange lines in (b) and (c)). The seismic observations in (b) and (c) are the same as in Figs. 5e and 5f, respectively.

of 2 cm/yr. We constrain the melt fraction to <0.3%, which is the suggested melt fraction for the asthenosphere (e.g., Selway and O'Donnell, 2019; Debayle et al., 2020). This small amount of melt reduces the viscosity of the asthenosphere only slightly, by a factor of ~0.98 (Fig. S7c, Supplementary Information F.4), when using olivine flow laws (Equations (5.3), (5.4) and (6)). Thus, grain-size insensitive dislocation creep remains dominant and the upper mantle flow and grain size profiles are unchanged (Fig. S7). However, the additional melt does reduce the seismic Q and $V_S$ (orange lines, Figs. 6b and 6c), which improves the fit to observations for our predicted seismic depth profiles. Here we have computed the effect of melt using Chantel et al. (2016), although this parameterization likely does not probe the grain-scale mechanisms that cause attenuation in the seismic frequency band. This adds uncertainty into our inference; however, we note that the recent Chantel et al. (2016) parameterization agrees with Faul et al. (2004).

### 5.3. Comparing flow-induced anisotropy with observations of seismic anisotropy

Seismic (radial and azimuthal) anisotropy is controlled by mantle rheology and fabric. Commonly, seismic anisotropy is attributed to olivine LPO that develops due to dislocation creep. Although different slip systems or deformation patterns (i.e., A-, C- and E-type) result in different magnitudes of radial and azimuthal anisotropy (e.g., Karato et al., 2008), anisotropy observations may add additional constraints for inferring mantle flow patterns (e.g., Lin et al., 2016; Russell et al., 2019). In particular, azimuthal anisotropy, which can be resolved on short length scales, is useful for inferring dynamics associated with lithospheric fabrics (e.g., Russell et al., 2019).

Since our analytical flow model is incapable of modeling olivine fabrics, we opt not to quantify predictions of radial or azimuthal anisotropy. Instead, we assume that the mantle will be strongly anisotropic under dislocation creep ($\dot{\varepsilon}_{disl} > \dot{\varepsilon}_{diff}$, following Behn et al. (2009)), which should be the dominant deformation mechanism for either dry or wet upper mantle below a 60 Myr old plate (Fig. 7b). For wet upper mantle, the $\dot{\varepsilon}_{disl}$ profile is dominated by the *PFn3* configuration (solid blue line, Fig. 7a), which mimics the global radial anisotropy trend (solid green line). Here a minimum $\dot{\varepsilon}_{disl}$ is evident at the base of the asthenosphere where weak fabric development may be attributed to weak, flow-induced

stresses. In contrast, a *CF* configuration, which is consistent with a dry upper mantle, does not produce a minimum at the base of the asthenosphere (dotted red line, Fig. 7a), consistent with seismic anisotropy beneath old oceanic plates (dotted green line). This may indicate that upper mantle beneath old oceanic plates is more *CF*-dominated than beneath younger plates.

## 6. Discussion

### 6.1. Assumptions and limitations

In this 1-D analytical study, we assume a composite rheology for olivine to represent the bulk rheology above 410 km since olivine is the most abundant and well-studied mineral. The viscosities of other phases such as pyroxenes (e.g., Chen et al., 2006) and the effect of multiple phases on overall rheology may additionally affect the predicted flow type. We furthermore assume that the MTZ has constant viscosity and flows under diffusion creep (*PFn1*-dominated). If the MTZ instead flows under dislocation creep with the wet upper mantle above it (entirely *PFn3*-dominated above 670 km), grain-sizes and predicted Q may increase below the asthenosphere due to low stresses induced by the *PFn3* configuration.

Empirically, seismic Q increases with increasing grain size (e.g., Jackson and Faul, 2010) but the magnitude of the minimum Q in the asthenosphere is not well constrained by observations. There may be other factors influencing attenuation that we ignore, such as oxygen fugacity decreasing below the asthenosphere, which can increase Q (e.g., Cline et al., 2018). As for the anelastic effect of melt, we have used the Chantel et al. (2016) parameterization, which mainly models a poroelastic effect and not grain-scale processes like grain boundary sliding or melt squirt. Faul et al. (2004) investigate the effect of melt on shear wave attenuation through torsional experiments, which suggest grain-boundary sliding as a candidate mechanism for the observed dissipation peak, and their results match the general trend of Chantel et al. (2016). This indicates that the parametrization of Chantel et al. (2016) may be valid for our purpose, but we also acknowledge its limitations. As of now, we do not have a unified anelasticity model that includes all sources. This would be complicated to construct because different sources do not independently affect seismic observations and some regions of the mantle may have different mechanisms for attenuation. In addition, we consider a single geological setting that
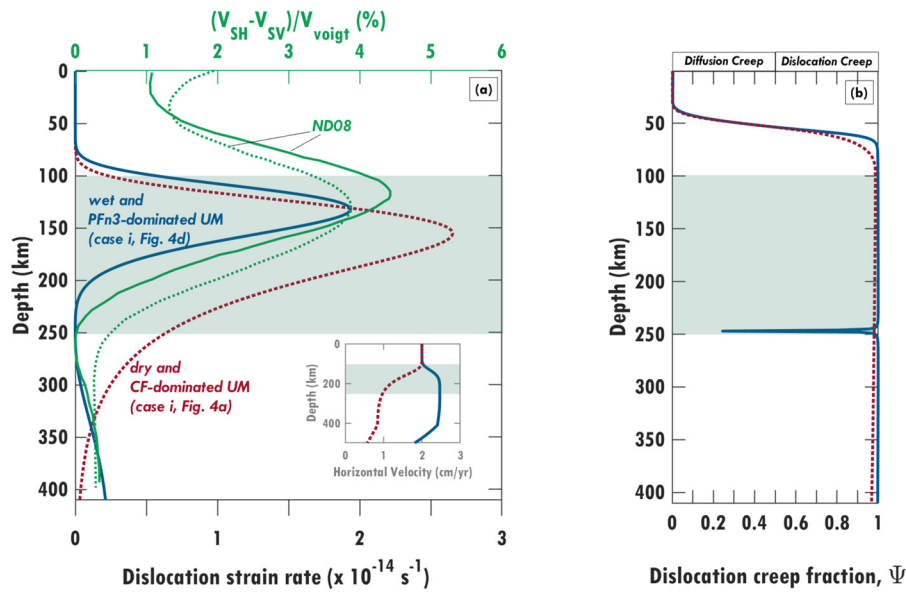
**Fig. 7. Patterns of upper mantle anisotropy** can be inferred from dislocation strain rates (a) and dominant deformation mechanisms (b) for dry (dotted red line) and wet (solid blue line) conditions with corresponding flow configurations shown in the inset. The dislocation strain rates are calculated for 60 Myr old lithosphere that is moving with a speed of 2 cm/yr above a −1 kPa/km pressure gradient in the underlying mantle (case i in Figs. 4a and 4d). The global seismic radial anisotropy models (ND08) (green lines in panel a, with corresponding top axis) are from Nettles and Dziewonski (2008) for mid-age (solid line) and old (dotted line) oceans. Abbreviations: *CF* = Couette flow, *PFn3* = plug flow, UM = upper mantle.

is not perfectly comparable with spherically averaging of the seismic observations, which may cancel out heterogeneities. Averaging our predicted seismic profiles across a range of imposed plate velocities and pressure gradients may improve the usefulness of our theoretical seismic models for comparison to globally-averaged observations.

The depth of the base of the asthenosphere and the velocity boundary conditions there are not well constrained. This is why we extend our 1-D model to 670 km, which should reduce any boundary effects. However, we have found that the rheology contrast between the MTZ and the overlying upper mantle significantly affects the distribution of flow between these layers (Fig. S6) and is poorly constrained. Furthermore, the rheology of the MTZ and the overlying upper mantle may vary laterally because of heterogeneous hydration of the transition zone (e.g., Karlsen et al., 2019). Lateral and radial variations of water content in the upper mantle may affect flow patterns and thus seismic Q. Constraints on upper mantle water content, for example from magnetotelluric (MT) surveys (e.g., Selway et al., 2019), may improve our forward models.

Since we consider 1-D mantle flow, we assume that pressure-driven flow moves in the same direction as the surface plate. However, any transverse component of the pressure gradient relative to the plate motion (essentially a 2-D problem) will affect the interaction between the two flows, particularly for non-Newtonian rheology (Natarov and Conrad, 2012). The resulting 2-D variations could impact predictions of grain size, seismic velocity, attenuation and anisotropy (e.g., Lin et al., 2016; Russell et al., 2019), but are beyond the scope of this study.

*6.2. Water, melt and grain size: Their interactions and impacts on mantle deformation*

Water content interacts with grain-sizes and melt content, affecting rheology in different ways. Generally, water content weakens mantle minerals, thus decreasing viscosity (e.g., Mei and Kohlstedt, 2000; Chen et al., 2006) and promoting faster deformation, particularly for dislocation creep. Depending on the strength of deformation, water may promote grain growth when deformation is weak or it may suppress grain growth when de-

formation is strong. If grain growth is suppressed resulting in sufficiently small steady-state grain sizes (<3 mm), diffusion creep may dominate. In our calculations, we obtained steady state grain sizes >3 mm favoring dislocation creep, potentially because we chose a small value for the activation volume for grain growth ($V_g = 4 \times 10^{-6}$ m$^3$/mol, Supplementary Fig. S2a or S2c).

Water promotes melting and preferentially partitions into melt (e.g., Katz et al., 2003; Koga et al., 2003; Hirschmann, 2010), which can migrate faster for larger grain size (Wark et al., 2003). Our flow models predict minimum grain sizes of ∼5–40 mm in the upper mantle (Fig. 4; encompasses the predictions of Behn et al. (2009)), which suggests a more permeable mantle for melt migration compared to geodynamic studies that assume ∼1 mm grain size for estimating melt permeability (e.g., Spiegelman and Kelemen, 2003; Cagnioncle et al., 2007). If this more permeable mantle allows melt to migrate away, the resulting dehydrated mantle rock may have elevated viscosity that promotes *CF* with relatively smaller grain sizes compared to upper mantle that retains its melt and water, which deforms by *PFn3* (Fig. 4). However, if the melt does not completely migrate away, such an increase in mantle viscosity may be offset by viscosity reduction due to melt that in turn facilitates faster deformation and may promote pressure-driven flow depending on the amount, distribution, and interconnectivity of melt. Here we only considered a small melt fraction (<0.3%, Fig. 6a), which is detectable by geophysical surveys but has a negligible impact on the viscosity and flow configuration (Fig. S7). However, this minor melt fraction can potentially affect asthenospheric deformation if the melt is aligned (e.g., Wang et al., 2013; Hansen et al., 2021) and it may have a significant impact on diffusion creep viscosity if the melt is well-connected (e.g., Holtzman, 2016).

*6.3. Constraints from regional seismic studies*

Our flow models, which assume globally-averaged conditions (e.g., for the mantle geotherm) and constant water content and pressure gradient across the upper 670 km, usefully predict globally-averaged seismic observations (e.g., for the LVZ or LQZ, Fig. 5). However, predictions from these models may not match regional seismic observations from particular locations, such as of
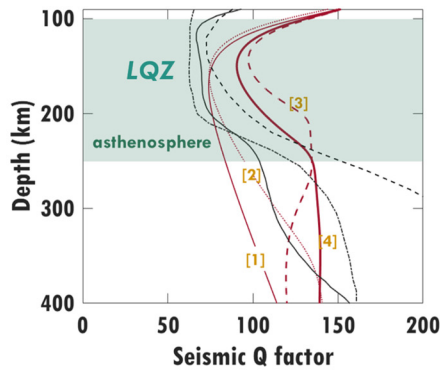
## (a) Flow configurations in the uppermost 670 km
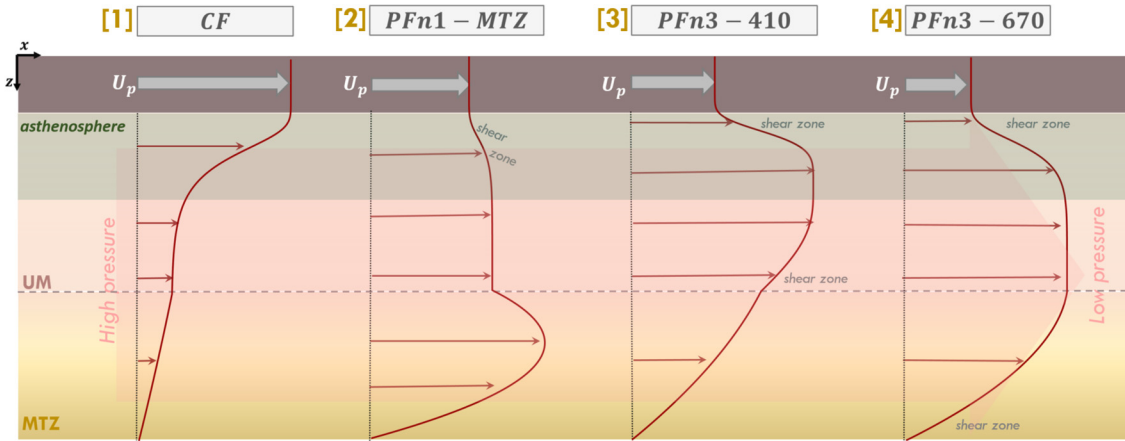


## (b) Different conditions to produce the different flow configurations
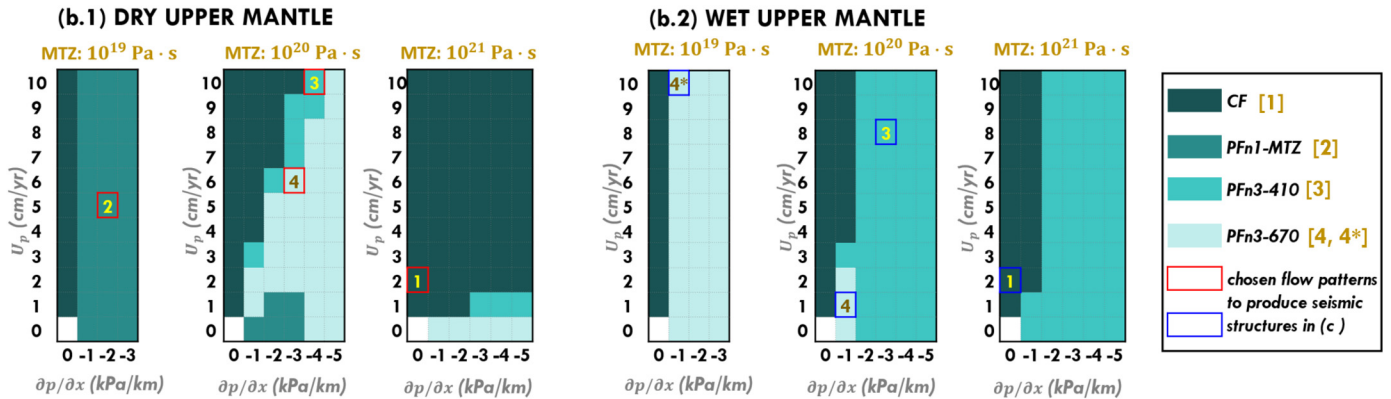


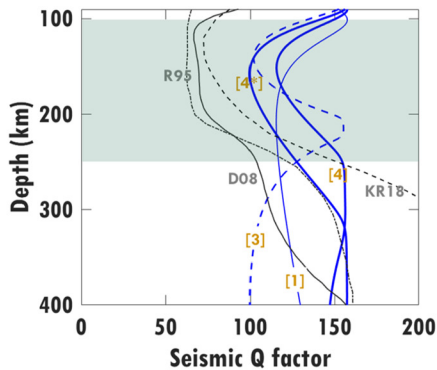## (c) Seismic Q produced by the different flow configurations



**Fig. 8. Upper mantle flow configurations.** (a) Schematic diagram showing different flow configurations that may dominate in the oceanic upper mantle and MTZ. (b) The dominant flow for different plate velocity ($U_p$) and horizontal pressure gradient ($\partial p/\partial x$) combinations for (b.1) dry (50 ppm H/Si) and (b.2) wet (1000 ppm H/Si) conditions, for different MTZ viscosities. (c) Predictions of seismic Q factor for different flow configurations for (c.1) dry and (c.2) wet conditions, where the type of flow configuration from (a) is indicated by a label [1]–[4] from (b.1) and (b.2) that refers to the ($U_p$, $\partial p/\partial x$) combination used to drive the flow. The corresponding flow configurations, stress profiles, grain sizes and viscosity structures are shown in Figs. S8 and S9 for dry and wet conditions, respectively. Note that flow configuration [2] (*PFn1 − MTZ*) does not occur for wet conditions. Observations of seismic Q for comparison are the KR18 and R95 global Q models of Karaoglu and Romanowicz (2018) and Romanowicz (1995), respectively, and the D08 model of Dalton et al. (2008) for mid-age oceans. Abbreviations: UM = upper mantle, MTZ = mantle transition zone, LQZ = low Q zone, CF = Couette flow (see Fig. 2a), PF = Poiseuille flow (*PFn1* for Newtonian rheology and *PFn3* for power law rheology and plug flow, see Fig. 2b).

those Lin et al. (2016) and Russell et al. (2019) for the central Pacific. In such cases, special and specific assumptions may have to be included in the flow model (e.g., a hotter asthenosphere) to match the regional seismic anisotropy patterns. Complexities of the different slip systems for olivine (A-, E-, C-type) in the mantle should also be taken into account because these slip systems are activated differently in different environments (e.g., Karato et al., 2008). Regional- or local-scale constraints from ocean-bottom seismometer (OBS) seismic arrays constrain localized and well-resolved seismic heterogeneities (e.g., Russell et al., 2019). Thus, regional observations of seismic velocity, anisotropy, and/or attenuation should provide useful constraints on regional mantle flow, but models will be more accurate if heterogeneities in water content, temperature, or other controlling parameters can be constrained. Geophysical observations from MT, heat flow and gravity, as well as petrological constraints, should provide context for developing useful regional mantle flow models.

## 7. Flow configurations for the upper mantle

By examining a range of flow drivers, hydration states, and MTZ viscosity contrasts, we identify four possible flow configurations (Fig. 8a) that may be present above 670 km depth:

**[1] CF:** Couette flow dominates across the uppermost 670 km if the upper mantle and MTZ are both strongly viscous (e.g., if they are dry). This occurs if pressure gradients are not large enough to drive flow within the highly viscous upper mantle.

**[2] PFn1 − MTZ:** PFn1 dominates in the MTZ with little deformation in the upper mantle if the MTZ is significantly less viscous than the upper mantle. This is because higher viscosities in the upper mantle prevent deformation, which instead becomes concentrated within the MTZ that is assumed to have a Newtonian rheology (thus PFn1-dominated).

**[3] PFn3 − 410:** PFn3 (plug flow) occurs dominantly within the upper mantle (about 410 km) if the MTZ is more viscous than the upper mantle. Here deformation concentrates within the less viscous (typically wet) upper mantle, and the pressure gradient must be large enough that PFn3 exceeds CF.

**[4] PFn3 − 670:** PFn3 may dominate across the uppermost 670 km if both the upper mantle and MTZ have sufficiently low viscosities (e.g., if they are wet) to allow existing pressure gradients to drive flow, or if pressure gradients are large enough to overcome CF and drive PFn3 in a viscous (dry) upper mantle.

Because of its impact on viscosity, water content helps to determine the dominant flow configuration (Fig. 8b). A dry upper mantle (Fig. 8b.1) may exhibit any of the four flow configurations, depending on the viscosity of MTZ. A low-viscosity MTZ ($10^{19}$ Pa·s) exhibits dominantly PFn1 − MTZ, an intermediate viscosity ($10^{20}$ Pa·s) may produce any of the four configurations depending on flow drivers, and a highly viscous MTZ ($10^{21}$ Pa·s) is stiff enough to only produce the CF configuration. A wet upper mantle (Fig. 8b.2) produces dominantly PFn3 flow, either above 410 km if the MTZ is stiff enough to prevent deformation or above 670 km otherwise.

Seismic Q (Figs. 8c.1 and 8c.2) and velocity ($V_s$, not shown) depth profiles can potentially constrain mantle flow (Fig. S8 and S9). From our forward models, a dominant PFn3 − 670 configuration in the oceanic mantle above 670 km (solid lines labeled with [4], Fig. 8c) best explains the LQZ within the asthenosphere. For this PFn3 − 670 flow configuration, magnitudes of Q within the asthenosphere for dry upper mantle ([4], Fig. 8c.1) are closer to the observations than those for wet upper mantle (Fig. 8c.2) because of smaller dry olivine grain-sizes (<3 cm, Fig. S8c). However, the small grain sizes for this case are induced by dry conditions and minimal deformation in the asthenosphere (thick solid red line, Fig. S8a). This viscosity model instead predicts significant deformation across the transition zone, where mantle viscosity is

lowest (Fig. S8d), and contradicts common mantle viscosity models constrained by other independent observations (e.g., Forte and Mitrovica, 1996; Steinberger and Calderwood, 2006). In contrast, wet conditions induce significant deformation beneath the plate as facilitated by the low-viscosity asthenosphere (e.g., Richards et al., 2001) and a pronounced PFn3 mantle flow configuration (Fig. S9a). Although the predicted Q values in wet asthenosphere ([4] and [4*], Fig. 8c.2) are larger than those predicted for dry asthenosphere, the presence of melt (Fig. 6b) or a larger assumed activation volume for grain growth (Fig. S2d) may reduce Q further. We also note that the PFn3 − 670 flow configuration produces large grain sizes beneath the asthenosphere, associated with minimal deformation there, and thus explains the large observed Q below 250 km (Fig. 8c). This is especially true for wet conditions, which produce larger Q values than dry conditions. For these reasons, we suggest that wet conditions better explain patterns of upper mantle deformation and the seismic observations (particularly Q) associated with them.

## 8. Conclusions

As a summary, we propose the following to explain the observed seismic depth profiles of the upper mantle, particularly the observed LQZ (low-Q zone; zone of high seismic attenuation):

(i) Poiseuille flow (PF, pressure-driven flow), and particularly plug flow (PFn3 for power-law rheology), may dominate deformation within the oceanic upper mantle. Wet conditions facilitate this type of flow because they reduce upper mantle viscosity, allowing ambient mantle pressure gradients to drive plug flow that overprints plate-driven shearing (Couette flow, CF). On the other hand, CF dominates if the upper mantle is dry and viscous.

(ii) Variations in grain size induced by plug flow (PFn3) are necessary to explain the LQZ in the asthenosphere. Here, low Q can be attributed to grain-size reduction due to extensive shearing within the low viscosity asthenosphere.

(iii) Seismic observations of large Q beneath the asthenosphere can be explained by large grain-sizes (>4 cm), which can be enhanced by wet conditions (Fig. 8c.2) and are associated with minimal deformation within the ∼250-410 km depth range. Such slow deformation is consistent with plug flow spanning the entire upper mantle and MTZ (the PFn3 − 670 flow configuration, Fig. 8a).

(iv) Melt in the asthenosphere is not necessary to explain observed seismic anomalies there (e.g., Lin et al., 2016). Instead, grain-size variations associated with plug flow (PFn3) can explain both the LQZ (Fig. 8c) and LVZ. Small amounts of melt can, however, amplify these trends, which can improve the fit to global seismic observations (e.g., Fig. 6).

Pressure-driven flow traveling beneath the oceanic lithosphere is important because it promotes long-wavelength mantle convection (Semple and Lenardic, 2018), drives tectonic plate motions (Semple and Lenardic, 2020), transports geochemical heterogeneities (Yamamoto et al., 2007), and generates intraplate volcanism (Ballmer et al., 2013). Here we have shown that pressure-driven plug flow (PFn3) may additionally explain pervasive seismic observations such as the LVZ and the LQZ by reducing asthenospheric grain-sizes. Because this grain-size reduction also weakens asthenospheric rocks, plug flow helps to maintain a low-viscosity asthenosphere, a key feature of Earth's interior structure that regulates a variety of geodynamic process ranging from plate tectonics to postseismic and postglacial relaxation (e.g., Richards and Lenardic, 2018).

## CRediT authorship contribution statement

**Florence D.C. Ramirez:** Formal analysis, Investigation, Methodology, Visualization, Writing – original draft. **Clinton P. Conrad:** Funding acquisition, Supervision, Writing – review & editing. **Kate Selway:** Funding acquisition, Supervision, Writing – review & editing.

## Declaration of competing interest

The authors declare that they have no known competing financial interests or personal relationships that could have appeared to influence the work reported in this paper.

## Data availability

No data was used for the research described in the article.

## Appendix A. Supplementary material

Supplementary material related to this article can be found online at https://doi.org/10.1016/j.epsl.2023.118232.

## References

Austin, N.J., Evans, B., 2007. Paleowattmeters: a scaling relation for dynamically recrystallized grain size. Geology 35, 343–346. https://doi.org/10.1130/G23244A.1.

Ballmer, M.D., Conrad, C.P., Smith, E.I., Harmon, N., 2013. Non-hotspot volcano chains produced by migration of shear-driven upwelling toward the East Pacific Rise. Geology 41, 479–482. https://doi.org/10.1130/g33804.1.

Becker, T., 2006. On the effect of temperature and strain-rate dependent viscosity on global mantle flow, net rotation, and plate-driving forces. Geophys. J. Int. 167, 943–957. https://doi.org/10.1111/j.1365-246X.2006.03172.x.

Behn, M., Hirth, G., Elsenbeck II, J.R., 2009. Implications of grain size evolution on the seismic structure of the oceanic upper mantle. Earth Planet. Sci. Lett. 282, 178–189. https://doi.org/10.1016/j.epsl.2009.03.014.

Cagnioncle, A.-M., Parmentier, E.M., Elkins-Tanton, L.T., 2007. Effect of solid flow above a suducting slab on water distribution and melting at convergent plate boundaries. J. Geophys. Res., Solid Earth 112, B09402. https://doi.org/10.1029/2007JB004934.

Chantel, J., Manthilake, G., Andrault, D., Novella, D., Yu, T., Wang, Y., 2016. Experimental evidence supports mantle partial melting in the asthenosphere. Sci. Adv. 2, e1600246. https://doi.org/10.1126/sciadv.1600246.

Chen, S., Hiraga, T., Kohlstedt, D.L., 2006. Water weakening of clinopyroxene in the dislocation creep regime. J. Geophys. Res. 111 (B8), B08203. https://doi.org/10.1029/2005JB003885.

Cline II, C., Faul, U., David, E., Berry, A., Jackson, I., 2018. Redox-influenced seismic properties of upper-mantle olivine. Nature 555, 355–358. https://doi.org/10.1038/nature25764.

Dalton, C., Ekström, G., Dziewonski, A., 2008. The global attenuation structure of the upper mantle. J. Geophys. Res. 113, B09303. https://doi.org/10.1029/2007JB005429.

Dalton, C., Ekström, G., Dziewonski, A., 2009. Global seismological shear velocity and attenuation: a comparison with experimental observations. Earth Planet. Sci. Lett. 284, 65–75. https://doi.org/10.1016/j.epsl.2009.04.009.

Debayle, E., Bodin, T., Durand, S., Ricard, Y., 2020. Seismic evidence for partial melt below tectonic plates. Nature 586, 555–559. https://doi.org/10.1038/s41586-020-2809-4.

Faul, U., Fitz Gerald, J.D., Jackson, I., 2004. Shear wave attenuation and dispersion in melt-bearing olivine polycrystals: 2. Microstructural interpretation and seismological implications. J. Geophys. Res., Solid Earth 109, B06202. https://doi.org/10.1029/2003JB002407.

Faul, U., Jackson, I., 2005. The seismological signature of temperature and grain size variations in the upper mantle. Earth Planet. Sci. Lett. 234, 119–134. https://doi.org/10.1016/j.epsl.2005.02.008.

Forte, A., Mitrovica, J., 1996. New inferences of mantle viscosity from joint inversion of long-wavelength mantle convection and post-glacial rebound data. Geophys. Res. Lett. 23, 1147–1150. https://doi.org/10.1029/96GL00964.

Forsyth, D.W., 1992. Geophysical constraints on mantle flow and melt generation beneath mid-ocean ridges. In: Mantle Flow and Melt Generation at Mid-Ocean Ridges, vol. 71, pp. 1–65.

Gutenberg, 1959. Physics of the Earth's Interior. Springer, New York.

Hall, C., Parmentier, E.M., 2003. Influence of grain size evolution on convective instability. Geochem. Geophys. Geosyst. 4, 1029. https://doi.org/10.1029/2002GC000308.

Hansen, L., Faccenda, M., Warren, J., 2021. A review of mechanisms generating seismic anisotropy in the upper mantle. Phys. Earth Planet. Inter. 313, 106662. https://doi.org/10.1016/j.pepi.2021.106662.

Hirschmann, M., 2010. Partial melt in the oceanic low velocity zone. Phys. Earth Planet. Inter. 179, 60–71. https://doi.org/10.1016/j.pepi.2009.12.003.

Hirth, G., Kohlstedt, D., 1996. Water in the oceanic upper mantle: implications for rheology, melt extraction and the evolution of the lithosphere. Earth Planet. Sci. Lett. 144 (1–2), 93–108. https://doi.org/10.1016/0012-821x(96)00154-9.

Hirth, G., Kohlstedt, D., 2003. Rheology of the upper mantle and the mantle wedge: a view from the experimentalists. In: Inside the Subduction Factory. In: Geophysical Monograph, vol. 138, pp. 83–105.

Höink, T., Lenardic, A., 2010. Long wavelength convection, Poiseuille–Couette flow in the low-viscosity asthenosphere and the strength of plate margins. Geophys. J. Int. 180, 23–33. https://doi.org/10.1111/j.1365-246X.2009.04404.x.

Holtzman, B., 2016. Questions on the existence, persistence, and mechanical effects of a very small melt fraction in the asthenosphere. Geochem. Geophys. Geosyst. 17, 470–484. https://doi.org/10.1002/2015GC006102.

Hua, J., Fischer, K.M., Becker, T.W., Gazel, E., Hirth, G., 2023. Asthenospheric low-velocity zone consistent with globally prevalent partial melting. Nat. Geosci. 16, 175–181. https://doi.org/10.1038/s41561-022-01116-9.

Jackson, I., Faul, U., 2010. Grainsize-sensitive viscoelastic relaxation in olivine: towards a robust laboratory-based model for seismological application. Phys. Earth Planet. Inter. 183, 151–163. https://doi.org/10.1016/j.pepi.2010.09.005.

Jung, H., Karato, S.-i., 2001. Water-induced fabric transitions in olivine. Science 293, 1460–1463. https://doi.org/10.1126/science.1062235.

Karaoglu, H., Romanowicz, B., 2018. Inferring global upper-mantle shear attenuation structure by waveform tomography using spectral element method. Geophys. J. Int. 213, 1536–1558. https://doi.org/10.1093/gji/ggy030.

Karato, S.-i., 1993. Importance of anelasticity in the interpretation of seismic tomography. Geophys. Res. Lett. 20, 1623–1626. https://doi.org/10.1029/93GL01767.

Karato, S.-i., 2012. On the origin of the asthenosphere. Earth Planet. Sci. Lett. 321–322, 95–103. https://doi.org/10.1016/j.epsl.2012.01.001.

Karato, S.-i., Jung, H., 1998. Water, partial melting and origin of the seismic low velocity and high attenuation zone in the upper mantle. Earth Planet. Sci. Lett. 157, 193–207.

Karato, S.-i., Jung, H., Katayama, I., Skemer, P., 2008. Geodynamic significance of seismic anisotropy of the upper mantle: new insights from laboratory studies. Annu. Rev. Earth Planet. Sci. 36, 59–95. https://doi.org/10.1146/annurev.earth.36.031207.124120.

Karlsen, K., Conrad, C., Magni, V., 2019. Deep water cycling and sea level change since the breakup of Pangea. Geochem. Geophys. Geosyst. 20, 2919–2935. https://doi.org/10.1029/2019GC008232.

Katz, R., Spiegelman, M., Langmuir, C., 2003. A new parametrization of hydrous mantle melting. Geochem. Geophys. Geosyst. 4 (9), 1073. https://doi.org/10.1029/2002GC000433.

Kaufmann, G., Lambeck, K., 2000. Mantle dynamics, postglacial rebound and the radial viscosity profile. Phys. Earth Planet. Inter. 121, 301–324. https://doi.org/10.1016/s0031-9201(00)00174-6.

Koga, K., Hauri, E., Hirschmann, M., Bell, D., 2003. Hydrogen concentration analyses using SIMS and FTIR: comparison and calibration for nominally anhydrous minerals. Geochem. Geophys. Geosyst. 4 (2), 1019. https://doi.org/10.1029/2002GC000378.

Lin, P.Y.P., Gaherty, J.B., Jin, G., Collins, J.A., Lizarralde, D., Evans, R.L., Hirth, G., 2016. High-resolution seismic constraints on flow dynamics in the oceanic asthenosphere. Nature 535, 538–541. https://doi.org/10.1038/nature18012.

Mei, S., Kohlstedt, D.L., 2000. Influence of water on plastic deformation of olivine aggregates: 2. Dislocation creep regime. J. Geophys. Res. 105, 21471–21481. https://doi.org/10.1029/2000JB900180.

Natarov, S., Conrad, C.P., 2012. The role of Poiseuille flow in creating depth-variation of asthenospheric shear. Geophys. J. Int. 190, 1297–1310. https://doi.org/10.1111/j.1365-246X.2012.05562.x.

Nettles, M., Dziewonski, A., 2008. Radially anisotropic shear velocity structure of the upper mantle globally and beneath North America. J. Geophys. Res. 113, B02303. https://doi.org/10.1029/2006JB004819.

Podolefsky, N.S., Zhong, S., McNamara, A.K., 2004. The anisotropic and rheological structure of the oceanic upper mantle from a simple model of plate shear. Geophys. J. Int. 158, 287–296. https://doi.org/10.1111/j.1365-246X.2004.02250.x.

Ramirez, F.D.C., Selway, K., Conrad, C.P., Lithgow-Bertelloni, C., 2022. Constraining upper mantle viscosity using temperature and water content inferred from seismic and magnetotelluric data. J. Geophys. Res., Solid Earth 127 (8), e2021JB023824. https://doi.org/10.1029/2021JB023824.

Richards, M., Yang, W.-S., Baumgardner, J., Bunge, H.-P., 2001. Role of a low-viscosity zone in stabilizing plate tectonics: implications for comparative terrestrial planetology. Geochem. Geophys. Geosyst. 2, 2000GC000115. https://doi.org/10.1029/2000GC000115.

Richards, M.A., Lenardic, A., 2018. The Cathles parameter (Ct): a geodynamic definition of the asthenosphere and implications for the nature of plate tectonics. Geochem. Geophys. Geosyst. 19 (12), 4858–4875. https://doi.org/10.1029/2018GC007664.

Ritterbex, S., Carrez, P., Cordier, P., 2020. Deformation across the mantle transition zone: a theoretical mineral physics view. Earth Planet. Sci. Lett. 547, 116438. https://doi.org/10.1016/j.epsl.2020.116438.

Romanowicz, B., 1995. A global tomographic model of shear attenuation in the upper mantle. J. Geophys. Res. 100 (B7), 12375–12394. https://doi.org/10.1029/95jb00957.

Russell, J.B., Gaherty, J.B., Lin, P.-Y.P., Lizarralde, D., Collins, J.A., Hirth, G., Evans, R.L., 2019. High-resolution constraints on Pacific upper mantle petrofabric inferred from surface-wave anisotropy. J. Geophys. Res., Solid Earth 124, 631–657. https://doi.org/10.1029/2018JB016598.

Selway, K., O'Donnell, J., 2019. A small unextractable melt fraction as the cause for the low velocity zone. Earth Planet. Sci. Lett. 517, 117–124. https://doi.org/10.1016/j.epsl.2019.04.012.

Selway, J., O'Donnell, J.P., Özaydin, S., 2019. Upper mantle melt distribution from petrologically constrained magnetotellurics. Geochem. Geophys. Geosyst. 20, 3328–3346. https://doi.org/10.1029/2019GC008227.

Semple, A., Lenardic, A., 2018. Plug flow in the Earth's asthenosphere. Earth Planet. Sci. Lett. 496, 29–36. https://doi.org/10.1016/j.epsl.2018.05.030.

Semple, A., Lenardic, A., 2020. The robustness of pressure-driven asthenospheric flow in mantle convection models with plate-like behavior. Geophys. Res. Lett. 47 (17), e2020GL089556. https://doi.org/10.1029/2020gl089556.

Shapiro, N.M., Ritzwoller, M.H., 2002. Monte-Carlo inversion for a global shear-velocity model of the crust and upper mantle. Geophys. J. Int. 151, 88–105. https://doi.org/10.1046/j.1365-246X.2002.01742.x.

Spiegelman, M., Kelemen, P., 2003. Extreme chemical variability as a consequence of channelized melt transport. Geochem. Geophys. Geosyst. 4, 1055. https://doi.org/10.1029/2002GC000336.

Steinberger, B., Calderwood, A., 2006. Models of large-scale viscous flow in the Earth's mantle with constraints from mineral physics and surface observations. Geophys. J. Int. 167, 1461–1481. https://doi.org/10.1111/j.1365-246X.2006.03131.x.

Tommasi, A., Tikoff, B., Vauchez, A., 1999. Upper mantle tectonics: three-dimensional deformation, olivine crystallographic fabrics and seismic properties. Earth Planet. Sci. Lett. 168, 173–186. https://doi.org/10.1016/S0012-821X(99)00046-1.

Turcotte, D., Schubert, G., 2014. Geodynamics, 3rd ed. Cambridge University Press, New York.

Wang, N., Montagner, J.P., Fichtner, A., Capdeville, Y., 2013. Intrinsic versus extrinsic seismic anisotropy: the radial anisotropy in reference Earth models. Geophys. Res. Lett. 40, 4284–4288. https://doi.org/10.1002/grl.50873.

Wark, D., Williams, C., Bruce Watson, E., Price, J., 2003. Reassessment of pore shapes in microstructurally equilibrated rocks, with implications for permeability of the upper mantle. J. Geophys. Res., Solid Earth 108 (B1), 250. https://doi.org/10.1029/2001JB001575.

Warren, J., Hirth, G., 2006. Grain size sensitive deformation mechanisms in naturally deformed peridotites. Earth Planet. Sci. Lett. 248, 438–450. https://doi.org/10.1016/j.epsl.2006.06.006.

Yamamoto, M., Phipps Morgan, J., Morgan, W.J., 2007. Global plume-fed asthenosphere flow—I: motivation and model development. In: Foulger, G.R., Jurdy, D.M. (Eds.), Plates, Plumes, and Planetary Processes: Geological Society of America Special Paper 430, pp. 165–188. https://doi.org/10.1130/2007.2430(09).